

# **Dynamical Characteristics of Planetary Penetrator: Effect of Incidence Angle and Attack Angle at Impact**

By

Hiroaki SHIRAISHI, Satoshi TANAKA, Masahiko HAYAKAWA,  
Akio FUJIMURA and Hitoshi MIZUTANI

(February 7, 2000)

**ABSTRACT:** A hard landing probe “penetrator” has been thought to be a very useful tool for planetary exploration, because it provides cost-effective capability of deploying scientific instruments on planetary surface and subsurface. But development of the penetrator for planetary exploration requires better understanding penetration dynamics in geological materials. The present paper describes some experimental results on the penetrator dynamics obtained during the course of the development of the LUNAR-A penetrator. Special emphasis is placed on understanding the effect of the oblique incidence and the attack angle of the penetrator on penetration depth and a final attitude at the rest position. Many impact experiments into a simulated lunar surface material are made using penetrators 30 mm in diameter, and the penetration characteristics (penetration path length and inflection angle) are investigated as functions of impact velocity, penetrator shape, impact angle and attack angle. The results indicate that the torque applied to the penetrator in cases of the impact with a finite attack angle changes the penetration characteristics significantly. The experimental data also suggests that the impact angle does not have a substantial effect on penetration path length and that the truncation of the nose tip from a conical nose is efficient to stabilize the penetration orientation.

## **1. INTRODUCTION**

Several planetary missions to use a hard landing probe, called a “penetrator” have been proposed (e.g., LUNAR-A, Deep Space 2, Mars-96, Rosetta). Utilization of penetrators for planetary exploration has many advantages over soft landing probes. The most obvious advantage of the penetrator will be its cost-effective capability of deploying scientific instruments on planetary surface. The penetrator will also make it possible to deliver scientific instruments into the planetary subsurface for in-situ chemical analysis and/or heat flow measurements, otherwise those measurements would require drilling holes from the surface.

The Institute of Space and Astronautical Science (ISAS) plans to undertake a lunar mission named as LUNAR-A, which will be launched by M-V launch vehicle of ISAS in 2002 fiscal year. The main objective of the LUNAR-A mission is to explore the lunar interior using seismometry and heat flow measurements. The scientific objectives would be almost impossible without penetrators under current severe mass and budget constraint of the LUNAR-A mission.

This paper will present some results of experiments made during the course of development of LUNAR-A penetrator. The LUNAR-A penetrator requires that it (the top of the penetrator) should rest in the lunar regolith at a depth deeper than 1 m and at attitude angle (angle between the penetrator body axis and the vertical) lower than 60 degrees. The first requirement comes from need of assuring temperature stability of the instruments and the second one comes from enabling measurement of heat flow and tele-communication between the penetrator and the mother orbiting spacecraft.

The depth and attitude of a penetrator after penetration are influenced by impact velocity, mass, cross-sectional area (base area), and nose-shape of the penetrator, mechanical properties of a target material, incidence angle, impact attack-angle, and others. Many experimental studies have been made to clarify the effects of those parameters on impact dynamics of penetrator penetration into geologic materials (e.g., [1][2][3][4]). However, almost all of these studies are limited to the case that the impact is normal to the target surface. Although normal incidence of the penetrator on the target simplifies the problem of penetrator dynamics, such an ideal condition is rarely met in actual planetary explorations; there always exists a possibility that the penetrator will hit on planetary surface at oblique incidence and with a finite attack-angle. Oblique impact with a finite attack-angle is inevitable for real missions due to slight (even if it may be small) error of separating the penetrator from the spacecraft, error of the attitude control of the penetrator, unexpected topography of planetary surface and others. Both the oblique incidence and a finite attack-angle will affect the penetration dynamics significantly because rotational torque will be applied to the penetrator at impact and during the course of penetration.

To date, as far as we know, the effects of oblique incidence and attack-angle on the penetration dynamics have not been investigated experimentally, possibly because it is difficult to simulate the impact condition with oblique incidence and attack-angle in a controlled fashion. In the present study, we report on the experimental setup to study these effects on penetration of a scale-model of LUNAR-A penetrator and results from the experiments.

## 2. EXPERIMENTAL METHOD

### 2.1. IMPACT EXPERIMENT APPARATUS

Impact experiments of the penetrators on lunar-regolith analogue target were made using a gun facility at the Institute of Space and Astronautical Science. The most important feature of this facility is that a gun to accelerate the scale-model of the penetrator itself is mounted on a rotation wheel driven by a hydraulic motor system (Figure 1).

The gun is a single stage powder gun about 90 cm in length and 30 mm in caliber. Since the gun can be rotated with the rotation wheel, we can change the incidence angle of the penetrator as well as the attack angle. The incidence angle is controlled by adjusting the timing of firing an explosive powder in respect to the rotation speed of the wheel and the attack angle is controlled by adjusting the impact speed and the rotation speed of the wheel. The target material, whose characteristics is described later, is a dry sand 70 cm in depth which is contained in a 2.5 m  $\times$  1.0 m  $\times$  0.9 m box. The impact velocity is measured by a magnet flyer method. About 5 g gun-powder (Winchester Co., Western Ball Powder 760) and a 1.5 mm thick A5052 aluminum diaphragm were required to accelerate a 350 g projectile to a velocity of about 150 m/s.

To accomplish a reliable shot (the incidence angle must be lower than 40°, otherwise the penetrator will be shot outside the sand container) from the rotating gun, an appropriate triggering method and the recording system were developed as shown in Figure 2.

A latching relay circuit is connected with an ignitor in the breech through a slip ring mounted on the spin motor. To trigger the ignitor, two optical spin sensors (Ono Sokki K.K., LG-916) and a



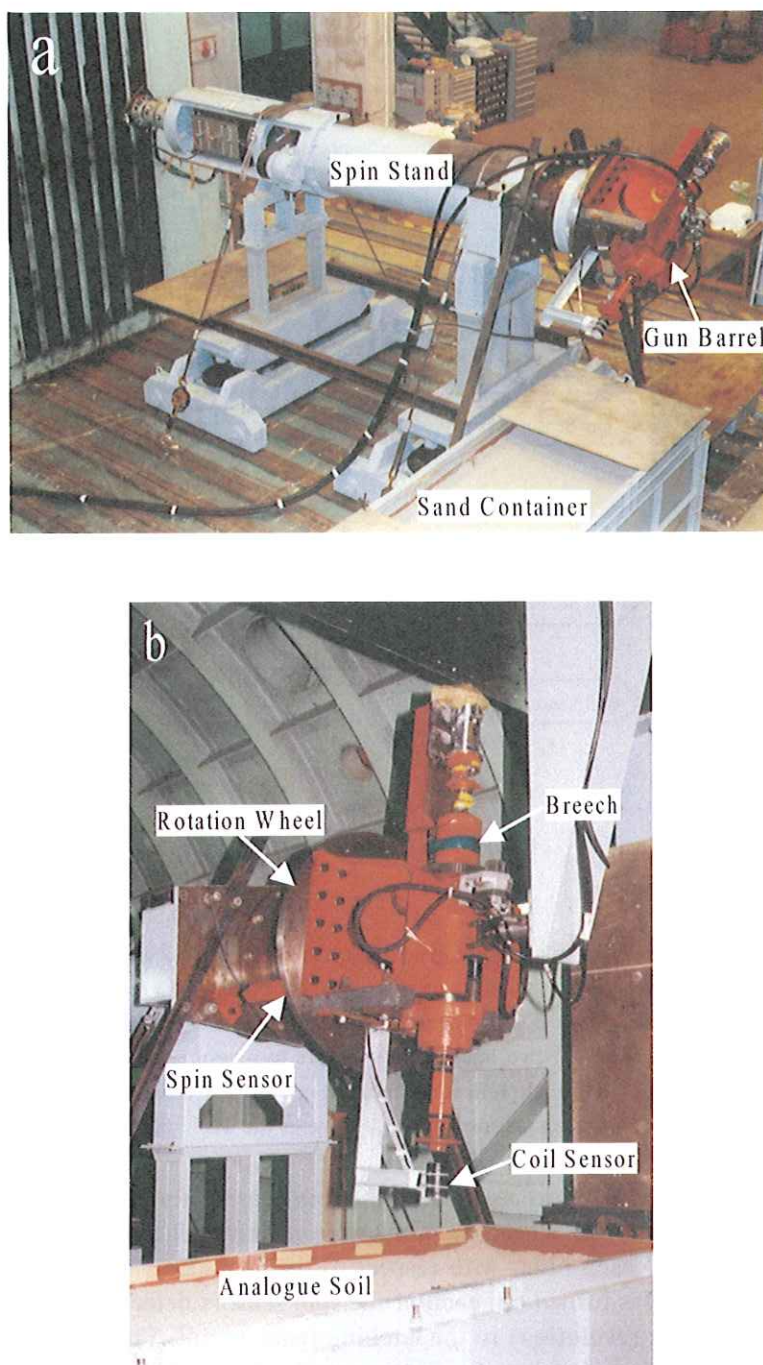


Fig. 1. (a) Photograph of the entire experiment facilities. The spin stand is seen at the central part, gun barrel at the right side, and sand container at the lower right side. (b) Photograph of the gun barrel mounted on the rotation wheel. A model penetrator and an ignitor are already set in the breech and not seen.

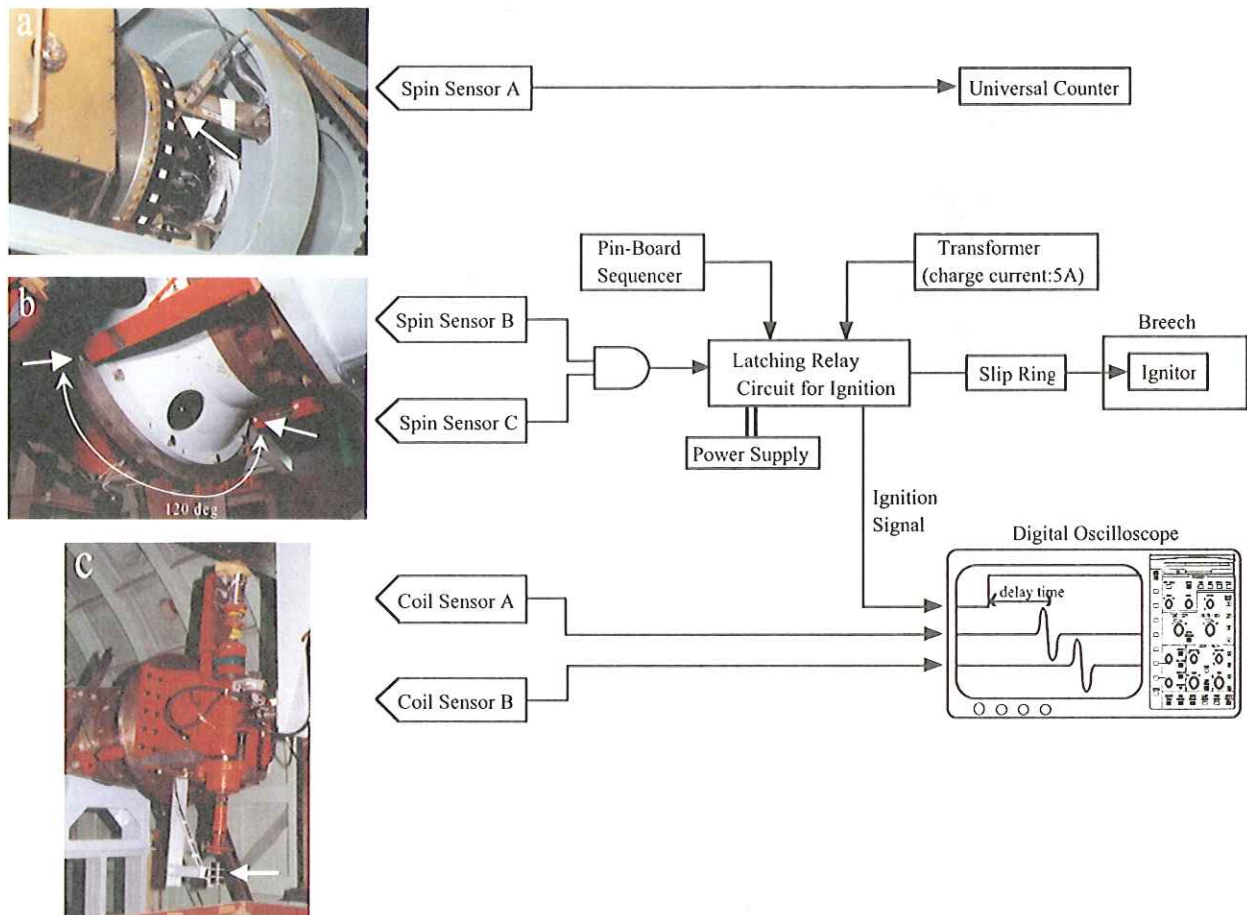


Fig. 2. Schematic diagram illustrating the trigger method and recording system. At the left side are shown the photographs of (a) an optical spin sensor and reflection markers to measure the wheel's spin rate, (b) two optical spin sensors for triggering, and (c) two magnet coil sensors to measure the impact velocity. In photograph (b), each reflection marker on the wheel's surface is viewed by separate optical spin sensors, which are set at the  $120^\circ$  phase angle.

pin-board sequencer (PRG-2018T) are used. Both the spin sensors are oriented parallel to the wheel's spin axis and point the edge of the wheel, 2 cm away from the surface (Figure 2b). They are set so as to make an angle of  $120^\circ$  each other with respect to the spin axis.

When the rotation wheel is turned on, each of the spin sensors detects the markers and sends the output signal (two times per revolution) to the latching relay circuit. The latching circuit supplies an ignition current to the ignitor, only when it simultaneously receives three trigger signals from the two spin sensors and from the sequencer. The ignition current of 5 A is discharged from a transformer.

Because LUNAR-A penetrator is planned to hit on the lunar surface at an impact angle of  $90^\circ$ , the shot must be adjusted so that the impacts are made at normal incidence. Considering a slight delay time from the ignition to the releasing of a penetrator from the gun barrel, we intentionally make the ignition slightly in advance, whose timing was determined by preliminary experiments; the time lag was obtained to be 30 to 40 milliseconds, which is equivalent to the  $63 \pm 9^\circ$  rotation angle in case of the spin rate of 5 Hz. This trigger method allowed us to control the impact angle ranging from  $80^\circ$  to  $100^\circ$  in almost all the experimental runs.

## 2.2. LUNAR ANALOGUE SOIL AS TARGET MATERIAL

It is known that the lunar surface is covered by the so-called “lunar regolith” of about 10 m thick which is a mixture of fine-powder soil and rock fragments (e.g., [5]). Because the mechanical properties of the target material could be essential parameters to affect the dynamic resistant force and the penetration characteristics, it is important to prepare a target having similar mechanical

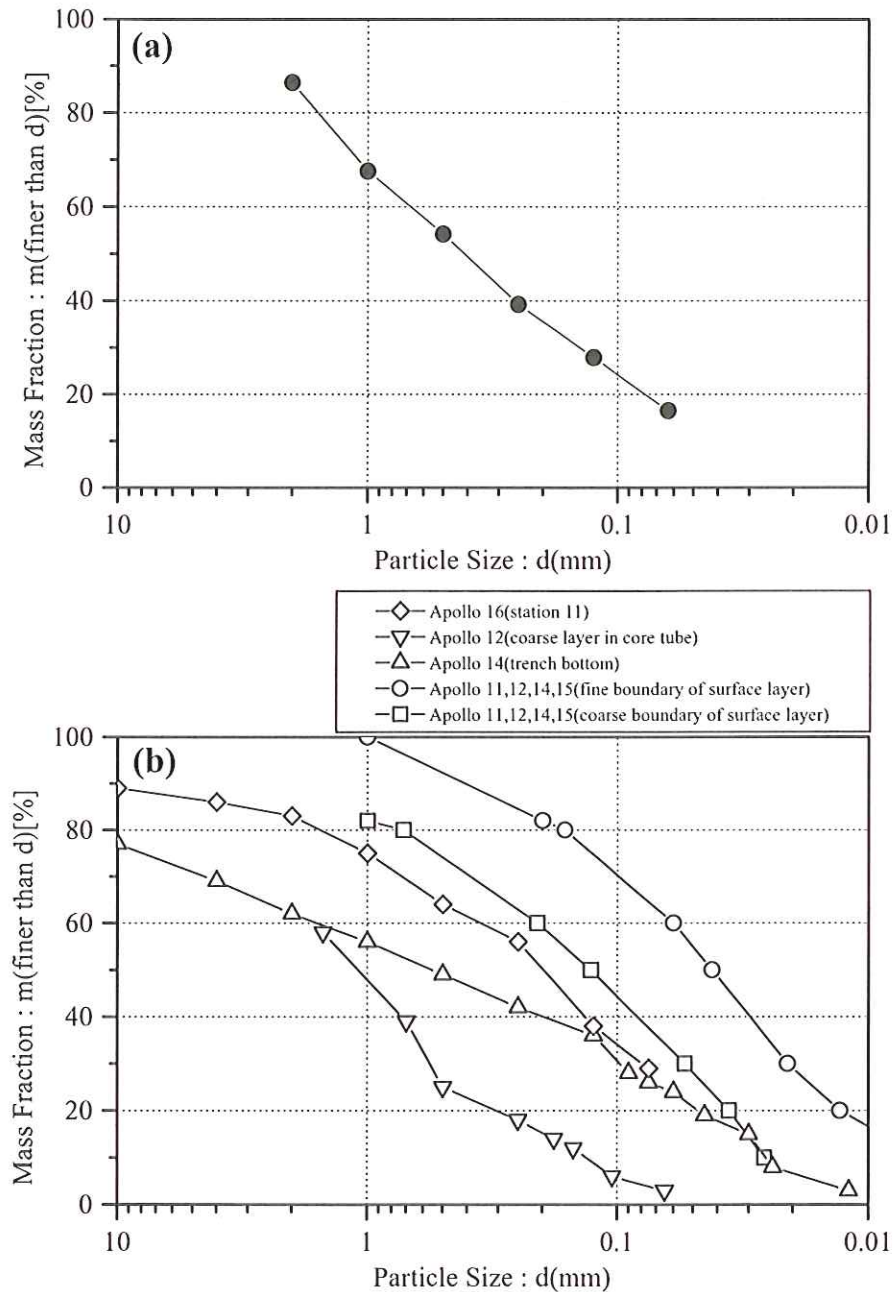


Fig. 3. Particle size distribution by sieve analysis: (a) lunar analogue soil used in this experiment; (b) Apollo lunar soil samples (adopted from [6]). The horizontal axis indicates the particle diameter and the vertical axis indicates weight percent finer than  $d$  mm.



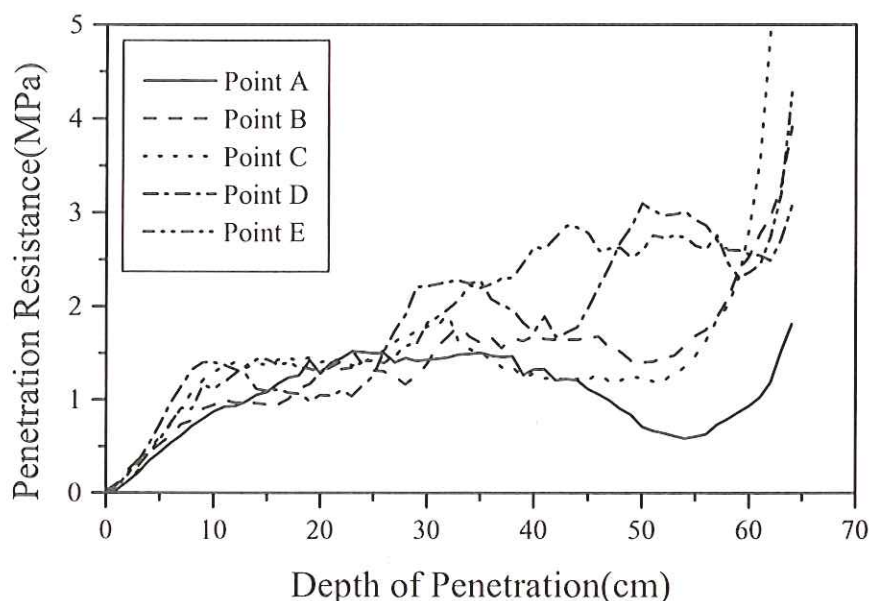


Fig. 4. One example of stress hardness data for the analogue soil sample measured by the cone-penetrometer system. These profiles are obtained at an every distance of 20 cm apart along the line including the spinning gun barrel. Point C lies in the perpendicular from the spin axis on the target surface and is nearest to the impact point.

properties to those of the lunar regolith.

We prepared a dry sand having a similar size distribution of particles to that of the lunar regolith. The relation of cumulative mass fraction with particle diameter in the present target material is shown in Figure 3. For comparison, the data for Apollo lunar soil samples are also indicated [6]. The specific gravity of the analogue soil was measured by means of a conventional water immersion pycnometry technique, and obtained a value of  $2.60 \pm 0.03$ . But the mechanical properties of granular media are more dependent on the bulk density or porosity than the true density. Therefore, we controlled the degree of compaction so that the bulk density and hardness of analogue soil were matched to those of lunar regolith as well as possible. The compaction was adjusted to make the hardness of the soil to be in a certain range of the values indicated by Apollo Soil Mechanics Experiments [7]. The resultant bulk density is in the range of 1.7 to 1.9 g/cm<sup>3</sup>. In order to secure the reproducibility of experiments, the hardness of the analogue soil was monitored by a static hardness test using a cone penetrometer similar to that used in the Apollo Soil Mechanics Experiments [7].

The equipment developed for characterizing the soil hardness consists of a cone-shaped penetrometer shaft with an apex angle of 40° and a base diameter of 12.7 mm and a recording system. The penetration of the penetrometer into the soil is manually operated at a constant velocity of 1 cm/s, and the resistance force is measured by a load cell mounted at the top of the shaft, which has a smaller diameter of 12 mm to reduce the skin friction. The movement of the penetrometer is measured with a DC potentiometer mounted at the shaft. Both outputs of the load cell and of the potentiometer are converted into digital data and stored in a personal computer through an interface board. As for the further details, see Report of the 9th Penetrator Impact Test [8]. One example of the results measured in this experiment is shown in Figure 4. This indicates that the average resistant force of the target sand is 0.5 to 2 MPa to the depth of 60 cm and that the hardness of this target material is very similar to that of the lunar regolith [7].

### 2.3. SHAPE AND SIZE OF THE MODEL PENETRATOR

The penetrators used in the present experiment are scale-models of about one-fifth of the flight model, and are made of A7075 aluminum. The shapes of penetrator models are shown in Figure 5. To investigate the effect of the nose shape on penetration characteristics, two models with two different nose shapes were prepared. One is of truncated conic shape with an apex angle of  $28.06^\circ$  and a height of 6 cm (hereafter abbreviated as STD, Figure 5a). Note that the ratio of the base diameter to the original nose length is one-half. The other is of truncated ogive-nose, which is more streamlined than the conic nose (hereafter abbreviated as OGIVE, Figures 5b and 5c). The curvature of the ogive shape is approximately expressed by the following equation,

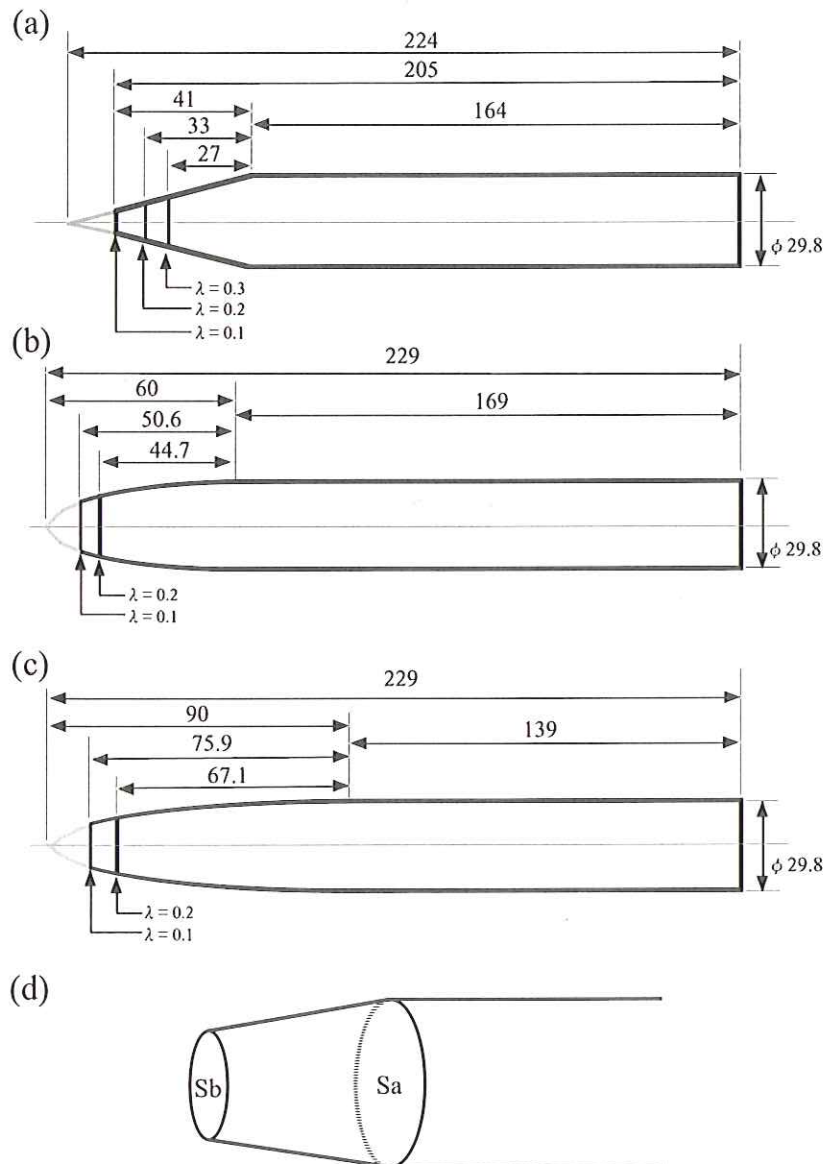


Fig. 5. Various shapes of penetrator models used in this experiment: (a) conical nose (STD); (b) ogive nose (OGIVE-60); (c) ogive nose (OGIVE-90). (d) A definition of  $\lambda$  ( $= S_b/S_a$ ) is schematically shown. The numbers in the figure indicate lengths in mm.

$$\left(\frac{2r}{D}\right) = \left[1 - \left(\frac{\phi}{\pi}\right) + \left(\frac{\sin 2\phi}{2\pi}\right)\right]^{\frac{1}{2}}; \cos \phi = \left(\frac{2X}{Ln}\right) - 1, \quad (1)$$

where  $Ln$  represents the nose length with no truncation,  $X$  distance from the apex,  $D$  base diameter (fixed to be 30 mm in the present experiments) and  $r$  radius at  $X$  ( $0 \leq X \leq Ln$ ). The OGIVE-60 and OGIVE-90 correspond to the cases of  $Ln = 60$  mm and 90 mm, respectively. As illustrated in Figure 5d,  $\lambda$  is the ratio of the nose sectional area with truncation to the base sectional area. Almost all the penetrator models used in the experiment have lengths of 19 cm to 28 cm and masses of 320 g to 380 g, respectively, resulting from the degree of truncation and from variation in the length of cylindrical part. Although the position of the center of gravity of the model was not controlled in this experiment, it is at about a half of the penetrator length as shown in Table 1 (the off-axis coordinate of the center of the gravity is thought to be negligibly small). To measure the impact velocity by the magnet flyer method, a small piece of Sm-Co magnet is mounted inside the rear end cap.

## 2.4. OBSERVED PARAMETERS

The coordinates for analysis of this experiment are illustrated in Figure 6 and Figure 7. In every experimental run, the following parameters were measured.

### 1. Impact Velocity: $V$

Impact velocity of a model penetrator is measured by recording the flight time difference between two coils mounted at a distance 10 cm apart (Figure 2c). The output signals of the

Table 1. Experimental Conditions and Results of Penetration Characteristics

Run No.	Penetrator Shape	Penetrator Mass (g)	Penetrator Length (cm)	Center of Gravity <sup>a</sup> (cm)	Impact Velocity (m/sec)	Stand Spin (rps)	Attack Angle (deg)	Impact Angle (deg)	Inflection Angle (deg)	Penetration Path Length (cm)
1	STD, $\lambda=0.1$	372	20.4	10.4	158	0.00	0.0	89.5	13.5	67.0
2	STD, $\lambda=0.2$	370	19.7	10.2	150	2.00	-3.2	86.7	-22.1	59.0
3	STD, $\lambda=0.3$	367	19.1	10.3	148	2.00	-3.2	91.1	-15.7	51.1
4	STD, $\lambda=0.1$	371	20.5	10.3	150	2.00	-3.2	91.2	-16.6	53.6
5	STD, $\lambda=0.1$	371	20.4	10.4	138	3.00	-5.2	86.4	-23.4	48.5
6	STD, $\lambda=0.2$	368	19.7	10.3	140	3.00	5.1	93.1	24.8	45.6
8	STD, $\lambda=0.3$	365	19.1	10.2	140	3.00	5.1	93.1	24.8	45.6
9	STD, $\lambda=0.1$	370	20.4	10.3	141	4.00	-6.7	78.7	-47.6	33.5
11	STD, $\lambda=0.3$	366	20.4	10.2	127	4.00	6.4	117.1	39.4	28.1
12	STD, $\lambda=0.2$	365	19.6	10.3	147	4.00	6.5	115.9	40.7	45.0
13	STD, $\lambda=0.1$	366	20.4	10.3	127	4.00	7.5	104.3	42.3	33.4
14	STD, $\lambda=0.2$	365	19.7	10.3	141	4.00	6.7	93.8	39.5	31.5
15	STD, $\lambda=0.3$	361	19.1	10.2	143	3.00	5.0	107.2	15.8	40.5
16	STD, $\lambda=0.2$	364	19.6	10.5	144	3.00	5.0	103.5	20.5	44.8
17	STD, $\lambda=0.1$	367	20.2	10.3	142	3.00	5.0	104.3	20.7	49.5
18	STD, $\lambda=0.2$	364	19.7	10.6	113	0.00	0.0	88.9	-3.2	44.7
19	STD, $\lambda=0.2$	364	19.6	10.4	117	0.00	0.0	89.9	-4.2	49.1
20	STD, $\lambda=0.2$	364	19.7	10.5	150	0.00	0.0	89.5	-7.5	50.6
28	STD, $\lambda=0.3$	363	19.1	10.3	111	0.00	0.0	90.0	9.0	37.0
29	STD, $\lambda=0.1$	368	20.5	10.6	112	1.95	4.1	93.9	28.0	36.1
30	STD, $\lambda=0.1$	368	20.5	10.3	112	1.95	4.1	93.9	28.0	36.1
31	STD, $\lambda=0.3$	342	24.7	13.0	116	0.00	0.0	89.6	0.6	43.7
32	STD, $\lambda=0.3$	363	19.1	10.6	106	2.00	-4.5	91.0	-22.5	33.1
33	STD, $\lambda=0.1$	368	20.5	10.5	111	4.96	-10.5	93.5	-27.6	33.2
34	STD, $\lambda=0.1$	368	20.5	10.4	111	5.00	-10.6	90.4	-30.3	24.7
35	STD, $\lambda=0.3$	360	24.7	13.2	125	0.00	0.0	89.4	3.4	43.7
36	STD, $\lambda=0.3$	363	19.1	10.2	114	4.99	10.3	109.7	27.7	34.6
37	STD, $\lambda=0.1$	368	20.5	10.3	120	4.99	9.8	104.0	27.2	37.3
38	STD, $\lambda=0.1$	367	20.4	10.4	102	4.02	-9.3	92.6	-24.1	23.9
40	STD, $\lambda=0.1$	367	20.5	10.4	149	5.48	8.7	110.4	28.2	43.9

<sup>a</sup> The center of gravity was measured from the rear end of penetrator.



Table 1. (continued)

Run No.	Penetrator Shape	Penetrator Mass (g)	Penetrator Length (cm)	Center of Gravity (cm)	Impact Velocity (m/sec)	Stand Spin (rps)	Attack Angle (deg)	Impact Angle (deg)	Inflection Angle (deg)	Penetration Path Length (cm)
41	STD, $\lambda=0.3$	363	19.1	10.2	143	5.52	9.1	102.9	26.0	39.2
42	STD, $\lambda=0.3$	366	24.7	13.0	104	2.01	-4.6	78.2	-16.2	29.5
45	STD, $\lambda=0.3$	363	19.1	10.4	148	5.52	-8.8	88.5	-20.7	31.3
46	STD, $\lambda=0.1$	367	20.5	10.5	152	5.53	8.6	96.0	27.4	41.5
47	STD, $\lambda=0.3$	363	24.7	12.9	101	2.05	-4.8	82.1	-7.8	31.8
48	STD, $\lambda=0.3$	366	24.7	13.3	107	4.03	-8.9	65.2	-25.9	25.0
49	STD, $\lambda=0.3$	363	19.1	10.3	106	5.51	12.2	99.3	23.8	25.7
50	STD, $\lambda=0.1$	367	20.5	10.5	106	5.53	12.2	100.9	23.6	31.8
51	STD, $\lambda=0.3$	366	24.7	13.2	117	0.00	0.0	90.0	-4.4	34.7
52	STD, $\lambda=0.3$	362	19.1	10.3	106	5.52	-12.2	85.3	-24.4	17.7
53	STD, $\lambda=0.3$	366	24.7	13.0	114	2.00	-4.2	83.0	-10.9	30.5
56	OGIVE-90, $\lambda=0.1$	325	21.5	10.1	158	0.00	0.0	89.8	4.8	54.1
58	OGIVE-60, $\lambda=0.1$	389	21.4	10.4	143	0.00	0.0	89.7	-10.3	66.4
60	OGIVE-90, $\lambda=0.2$	322	20.6	9.7	157	0.00	0.0	88.4	-15.6	62.4
62	OGIVE-60, $\lambda=0.2$	387	20.9	10.5	144	0.00	0.0	88.8	-9.9	61.3
67	OGIVE-90, $\lambda=0.2$	322	20.6	9.5	149	2.97	4.7	109.5	12.8	59.5
68	OGIVE-60, $\lambda=0.1$	389	21.0	10.4	145	2.97	4.9	108.0	14.5	60.9
70	OGIVE-90, $\lambda=0.1$	325	21.6	9.7	153	2.97	4.6	106.2	20.2	56.3
71	OGIVE-60, $\lambda=0.2$	333	20.8	10.7	160	0.00	0.0	89.7	8.0	57.5
72	OGIVE-90, $\lambda=0.2$	321	20.6	10.0	196	0.00	0.0	89.1	10.4	65.6
74	OGIVE-60, $\lambda=0.2$	333	20.9	10.8	149	4.97	7.9	109.9	12.9	48.3
75	OGIVE-90, $\lambda=0.1$	324	21.5	9.1	197	0.00	0.0	90.3	-13.6	60.9
77	OGIVE-60, $\lambda=0.1$	334	21.4	10.8	152	4.99	7.8	118.9	19.0	50.8
78	OGIVE-90, $\lambda=0.2$	321	20.6	9.6	151	5.01	-7.8	87.4	-22.1	52.6
79	OGIVE-90, $\lambda=0.1$	324	21.5	9.6	150	5.00	-7.9	92.8	-21.4	49.8
82	STD, $\lambda=0.2$	368	19.8	10.4	155	4.99	7.6	108.8	14.6	46.6
83	OGIVE-60, $\lambda=0.2$	332	20.9	10.6	148	4.99	8.0	103.7	19.0	38.8
84	OGIVE-90, $\lambda=0.2$	321	20.6	9.8	163	4.96	7.2	101.9	20.9	46.9
87	OGIVE-90, $\lambda=0.2$	321	20.6	9.6	200	4.98	5.9	100.2	24.2	58.2
96	OGIVE-90, $\lambda=0.2$	321	20.6	9.6	185	3.85	4.9	95.1	29.3	53.6
155	OGIVE-90, $\lambda=0.2$	354	27.0	11.8	105	0.00	0.0	88.8	11.1	68.3
156	OGIVE-90, $\lambda=0.1$	364	28.7	13.5	113	0.00	0.0	90.4	7.6	65.6
157	OGIVE-90, $\lambda=0.1$	364	28.7	13.5	116	0.00	0.0	48.6	5.9	76.3
158	OGIVE-90, $\lambda=0.1$	364	28.7	13.5	113	2.07	-4.3	69.0	-28.4	58.7
159	OGIVE-90, $\lambda=0.2$	348	27.1	12.2	110	0.00	0.0	90.1	7.9	59.9
160	OGIVE-90, $\lambda=0.2$	348	27.1	12.2	144	0.00	0.0	51.3	-0.3	79.0
162	OGIVE-90, $\lambda=0.2$	363	27.9	13.6	109	1.97	-4.3	76.4	-23.3	49.0
163	OGIVE-90, $\lambda=0.2$	354	27.2	12.1	144	0.00	0.0	90.8	-0.8	64.7
164	OGIVE-90, $\lambda=0.1$	364	28.7	13.5	83	3.03	-8.6	73.9	-30.9	38.5
165	OGIVE-90, $\lambda=0.1$	364	28.7	13.5	158	3.00	-4.5	87.0	-22.8	67.2
166	OGIVE-90, $\lambda=0.2$	363	27.9	13.6	109	3.00	-6.6	85.3	-28.5	53.9
167	OGIVE-90, $\lambda=0.2$	363	27.9	13.6	113	4.00	8.4	94.7	24.2	46.6
168	OGIVE-90, $\lambda=0.2$	351	27.1	12.0	150	0.00	0.0	87.9	-5.1	62.1
170	OGIVE-90, $\lambda=0.1$	329	28.8		158	0.00	0.0	87.8	-2.2	69.3
171	OGIVE-90, $\lambda=0.2$	363	27.9	12.0	115	0.00	0.0	90.2	5.8	58.8
172	STD, $\lambda=0.1$	329	28.7	13.4	127	0.00	0.0	47.6	8.6	51.9
173	STD, $\lambda=0.1$	329	28.7	13.4	118	0.00	0.0	47.8	4.8	51.4
174	OGIVE-90, $\lambda=0.2$	363	27.9	12.0	144	5.10	8.4	101.9	35.8	38.1
175	STD, $\lambda=0.1$	329	28.7	13.4	115	0.00	0.0	47.5	3.5	45.5
176	STD, $\lambda=0.1$	329	28.7	13.4	120	2.00	-4.0	84.5	-22.9	43.2
177	OGIVE-90, $\lambda=0.2$	320	27.8	12.8	115	0.00	0.0	90.6	1.4	50.4
178	OGIVE-90, $\lambda=0.2$	320	27.8	12.8	122	0.00	0.0	47.3	3.9	51.3
179	OGIVE-90, $\lambda=0.2$	320	27.8	12.8	114	2.02	-4.2	82.6	-23.2	45.3
180	OGIVE-90, $\lambda=0.2$	320	27.8	12.8	166	2.03	2.9	89.4	15.0	54.0
181	OGIVE-90, $\lambda=0.2$	320	27.8	12.8	158	2.00	3.0	89.9	20.4	59.1
182	OGIVE-90, $\lambda=0.2$	320	27.8	12.8	115	3.05	6.3	89.2	21.5	50.9
187	OGIVE-90, $\lambda=0.2$	320	27.9	12.8	106	5.00	-11.1	78.3	-29.3	49.6
188	OGIVE-90, $\lambda=0.2$	320	27.9	12.8	156	3.00	4.6	92.5	20.9	56.9
189	OGIVE-90, $\lambda=0.1$	321	28.8		106	0.00	0.0	89.1	-6.6	58.1
190	OGIVE-90, $\lambda=0.1$	321	28.8		120	3.05	6.0	89.4	26.3	52.5

Table 1. (continued)

Run No.	Penetrator Shape	Penetrator Mass (g)	Penetrator Length (cm)	Center of Gravity (cm)	Impact Velocity (m/sec)	Stand Spin (rps)	Attack Angle (deg)	Impact Angle (deg)	Inflection Angle (deg)	Penetration Path Length (cm)
191	OGIVE-90, $\lambda=0.1$	321	28.8		150	3.05	4.8	121.6	-3.1	40.4
193	OGIVE-90, $\lambda=0.1$	339	27.4	11.3	144	0.00	0.0	90.6	-0.6	61.9
194	OGIVE-90, $\lambda=0.1$	339	27.4	11.3	160	0.00	0.0	90.1	-0.1	66.4
195	OGIVE-90, $\lambda=0.1$	372	28.4	11.6	98	0.00	0.0	88.3	-1.7	66.4
196	OGIVE-90, $\lambda=0.1$	372	28.4	11.6	97	0.00	0.0	89.2	-0.8	62.4
198	OGIVE-90, $\lambda=0.1$	363	28.8	13.4	150	0.00	0.0	48.6	8.3	69.9
199	OGIVE-90, $\lambda=0.1$	363	28.8	13.4	153	0.00	0.0	44.4	8.1	83.4
200	OGIVE-90, $\lambda=0.1$	372	28.4	11.6	87	0.00	0.0	88.7	-1.4	55.4
201	OGIVE-90, $\lambda=0.1$	363	28.8	13.4	159	2.00	3.0	95.4	19.6	64.3
202	OGIVE-90, $\lambda=0.1$	363	28.8	13.4	168	0.00	0.0	47.2	9.8	85.5
203	OGIVE-90, $\lambda=0.1$	363	28.8	13.4	150	1.99	-3.2	85.3	-27.6	66.7
204	OGIVE-90, $\lambda=0.1$	363	28.8	13.4	146	3.01	4.9	91.6	21.5	64.9
205	STD, $\lambda=0.3$	347	27.4	13.7	117	0.00	0.0	47.1	5.0	53.9
206	STD, $\lambda=0.3$	347	27.4	13.7	153	0.00	0.0	48.2	1.9	54.7
207	OGIVE-90, $\lambda=0.1$	372	28.4	11.6	84	0.00	0.0	47.2	8.9	64.6
208	STD, $\lambda=0.3$	347	27.4	13.7	158	0.00	0.0	47.7	-1.3	55.6
209	OGIVE-90, $\lambda=0.1$	372	28.4	11.6	79	0.00	0.0	48.8	5.2	56.9
212	OGIVE-90, $\lambda=0.1$	380	28.4	12.2	91	0.00	0.0	47.4	9.1	55.3
213	STD, $\lambda=0.3$	355	22.5	8.4	140	0.00	0.0	47.2	-5.4	46.8
214	OGIVE-90, $\lambda=0.1$	380	28.4	12.2	96	2.00	-5.0	80.5	-23.6	46.2
216	STD, $\lambda=0.3$	354	22.5	8.4	193	0.00	0.0	46.1	15.1	57.5
217	OGIVE-90, $\lambda=0.1$	380	28.4	12.2	102	0.00	0.0	89.9	-0.1	52.9
219	STD, $\lambda=0.3$	354	22.5	8.4	144	5.00	-8.2	78.3	-37.1	34.7
220	OGIVE-90, $\lambda=0.1$	380	28.4	12.2	104	0.00	0.0	48.4	14.4	57.6
221	STD, $\lambda=0.3$	354	22.5	8.4	188	5.00	-6.3	84.4	-36.6	42.7
222	OGIVE-90, $\lambda=0.1$	380	28.4	12.2	98	3.00	-7.3	80.7	-29.3	50.1
223	OGIVE-90, $\lambda=0.1$	380	28.4	12.2	135	0.00	0.0	48.4	5.0	76.5
224	OGIVE-90, $\lambda=0.1$	364	28.8	13.4	150	3.00	4.8	87.8	22.8	57.9
225	OGIVE-90, $\lambda=0.1$	380	28.4	12.2	131	2.00	-3.6	83.3	-18.8	59.3
226	OGIVE-90, $\lambda=0.1$	380	28.4	12.2	136	2.00	3.5	89.3	13.6	64.8
227	OGIVE-90, $\lambda=0.1$	380	28.4	12.2	136	2.99	-5.2	87.1	-29.4	68.6
228	STD, $\lambda=0.3$	347	24.4	10.0	109	0.00	0.0	48.8	10.2	50.6
229	OGIVE-90, $\lambda=0.1$	364	28.8	13.4	160	1.98	2.9	90.3	20.5	71.8
230	STD, $\lambda=0.3$	347	24.4	10.9	105	0.00	0.0	47.0	8.7	53.9
234	OGIVE-90, $\lambda=0.1$	375	28.4	11.9	107	0.00	0.0	46.9	0.2	72.1
235	OGIVE-90, $\lambda=0.1$	375	28.4	11.9	113	4.10	-8.6	82.0	-35.1	51.9
236	OGIVE-90, $\lambda=0.1$	375	28.4	11.9	134	4.09	-7.2	86.0	-24.4	66.7
243	OGIVE-90, $\lambda=0.1$	383	29.0	12.0	131	2.90	-5.3	86.2	-16.5	71.4
244	OGIVE-90, $\lambda=0.1$	334	28.7	13.2	165	0.00	0.0	47.2	11.9	74.4
245	OGIVE-90, $\lambda=0.1$	382	29.0	12.0	125	4.05	-7.7	81.6	-26.7	65.4
246	OGIVE-90, $\lambda=0.1$	383	29.0	12.0	132	5.00	-8.9	81.5	-21.3	64.0
247	OGIVE-90, $\lambda=0.1$	375	28.4	12.4	116	2.01	-4.1	86.6	-20.0	61.0
248	OGIVE-90, $\lambda=0.1$	375	28.4	12.4	109	2.99	-6.5	74.0	-31.6	48.7
249	OGIVE-90, $\lambda=0.1$	375	28.4	12.4	115	2.95	-6.1	77.9	-32.3	53.9
250	OGIVE-90, $\lambda=0.1$	374	28.5	12.2	110	2.07	-4.5	81.6	-24.2	53.3
251	OGIVE-90, $\lambda=0.1$	374	28.5	12.2	116	3.02	-6.2	78.1	-28.4	57.0
252	OGIVE-90, $\lambda=0.1$	375	28.4	12.2	111	2.02	-4.3	81.7	-26.0	57.6
253	OGIVE-90, $\lambda=0.1$	375	28.4	12.2	108	2.98	-6.5	78.2	-33.6	58.1
254	OGIVE-90, $\lambda=0.1$	332	28.7	12.9	100	0.00	0.0	48.7	3.3	58.6
255	OGIVE-90, $\lambda=0.1$	375	28.4	12.2	137	3.04	-5.3	82.3	-28.8	57.7
256	OGIVE-90, $\lambda=0.1$	332	28.7	12.9	117	0.00	0.0	49.1	12.4	62.3
257	OGIVE-90, $\lambda=0.1$	332	28.7	12.9	113	0.00	0.0	49.2	1.5	64.1
259	OGIVE-90, $\lambda=0.1$	332	28.7	12.9	157	0.00	0.0	47.3	-8.3	72.9
263	OGIVE-90, $\lambda=0.1$	374	28.4	12.1	115	2.99	-6.2	81.8	-28.8	51.1
264	OGIVE-90, $\lambda=0.1$	374	28.4	12.1	114	2.02	4.2	95.1	22.3	58.0
265	OGIVE-90, $\lambda=0.1$	374	28.4	12.1	114	3.02	-6.3	86.3	-23.4	50.0
266	STD, $\lambda=0.3$	345	24.4	10.9	93	0.00	0.0	49.4	4.8	41.3
267	STD, $\lambda=0.3$	345	24.4	10.9	110	0.00	0.0	48.2	6.5	47.1



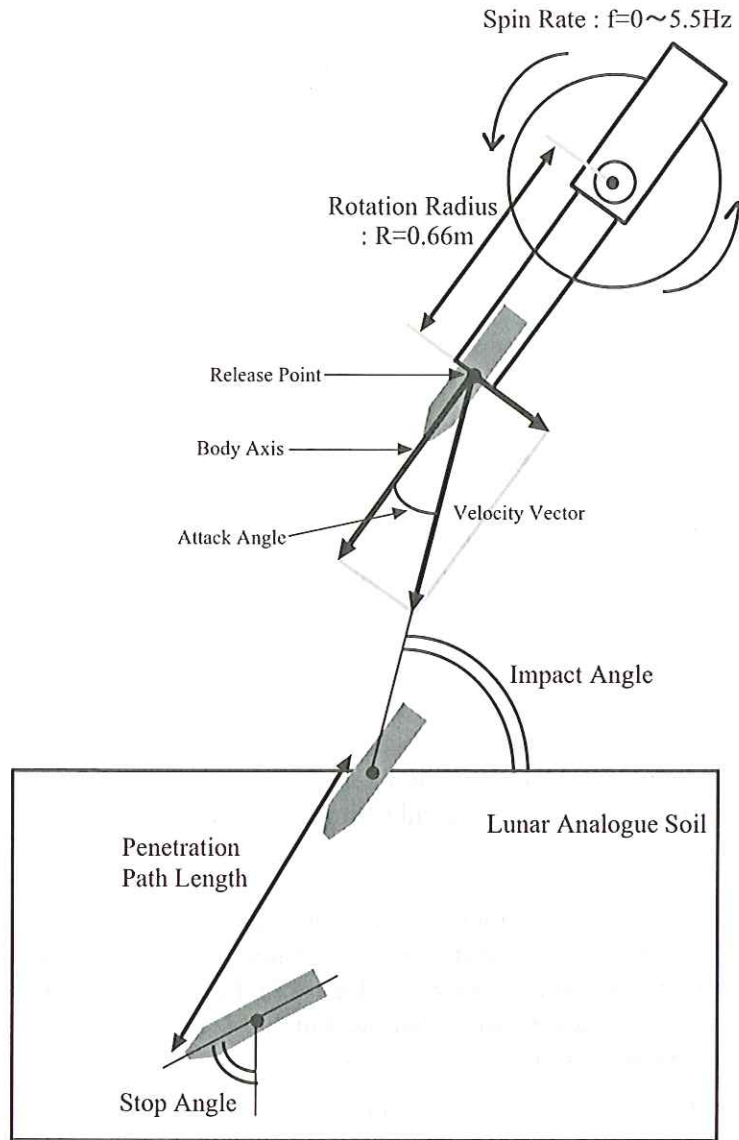


Fig. 6. Schematic diagram of impact experiment and coordinates for the measurement.

coils are stored in a digital storage oscilloscope (Nicolet, Model 490), together with the ignition timing signal. The error of the impact velocity is estimated to be  $\pm 5\%$ .

2. Spin Rate:  $f$

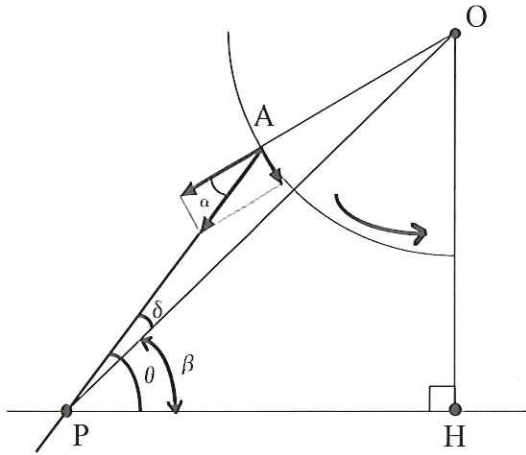
An optical spin sensor and a universal counter (IWATSU Electric Co., SC-7202) measure a spin rate of the gun barrel. Twenty-four reflection markers are stuck at every  $15^\circ$  on the periphery of the drum concentric with the wheel (Figure 2a). The signal detected by the spin sensor is sent to the universal counter, and the value shown on the panel is measured with the eye. The error of the spin rate is estimated to be less than 0.05 Hz.

3. Attack Angle:  $\alpha$

Attack angle is calculated by the following equation,

$$\tan \alpha = \frac{2\pi f R}{V}, \quad (2)$$

(a) Positive Attack Angle



(b) Negative Attack Angle

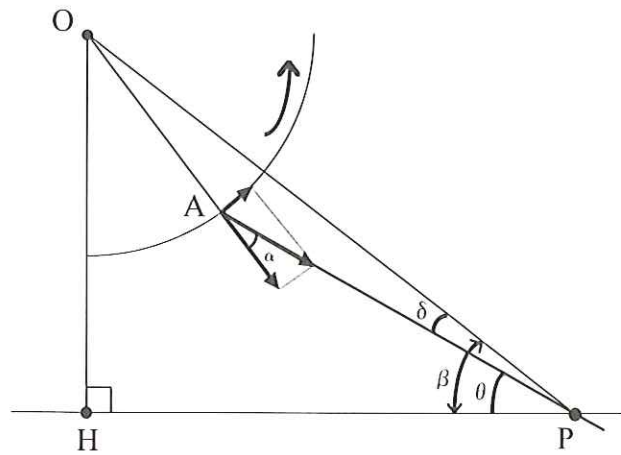


Fig. 7. Schematic diagram illustrating the relation of the attack angle and impact angle:  
(a) positive attack angle; (b) negative attack angle. As for the details of the calculation method of the impact angle, see text.

where  $f$  is spin rate [Hz],  $V$  is the impact velocity, and  $R$  is the rotational radius of 0.66 m (Figure 6). Because the gun barrel can be rotated at the maximum spin rate of 5.5 Hz, the attack angle up to  $8.6^\circ$  is attained in case of the impact velocity of 150 m/s. Considering the positional relation between body axis and velocity vector, we distinguish the positive attack angle and the negative attack angle as illustrated in Figure 7.

#### 4. Impact Angle: $\theta$

Impact angle is defined as an angle between the velocity vector of the penetrator and the horizontal surface. When a penetrator impacts at non-zero attack angle, the impact angle is determined using the following procedures (Figure 7). Let us denote that  $P$  is the impact point on the target,  $A$  is the release point from the gun and  $O$  is the center of the spinning wheel. From the geometrical relation,

$$\overline{OA} \sin (180^\circ - \alpha) = \overline{OP} \sin \delta, \quad (3)$$

where  $\alpha$  and  $\delta$  are the attack angle and the angle  $\angle APO$ , respectively. Because we can measure  $\overline{OP}$ ,  $\overline{OA}$ , and  $\alpha$ , the impact angle  $\theta$  is calculated by the equation,

$$\theta = \beta + \delta, \quad (4)$$

where  $\beta$  represents the angle  $\angle OPH$ . When a projectile is intended to be fired at zero attack angle, the gun barrel is fixed at the impact angle of  $50^\circ$  or  $90^\circ$ .

#### 5. Inflection Angle: $\Delta\phi$

When a penetrator collides in the oblique direction and/or at non-zero attack, it is expected to change its attitude during the course of penetration. The change of attitude of the penetrator is called to be the inflection angle here. The inflection angle  $\Delta\phi$  is calculated by the equation,

$$\Delta\phi = \theta - 90^\circ + \phi, \quad (5)$$

where  $\phi$  is the stop angle of the penetrator from the normal. The stop angle is measured by a clinometer (see also Figure 6).



### 6. Penetration Path Length: $d$

When a penetrator impacts in the oblique direction and/or at non-zero attack, its penetration path is thought to be curved. But it is difficult to infer the real curved path. Therefore we estimate the path length from a straight line drawn from the impact point to the head of a penetrator as illustrated in Figure 6. Thus it gives the minimum estimate of the real penetration path length. Impact point  $P$  is assumed to be the center of a crater produced by the impact penetration. The position of penetrator's tip is calculated by measuring the depth of penetrator's rear end and the stop angle, at which the penetrator came to rest in the sand.

All experiments were conducted under atmospheric conditions. Because the distance between the releasing point and impact points is less than 1 m in all experimental runs, the effect of aerodynamic force on the deceleration and disturbance of the tilt is assumed to be negligible. And also, it is assumed that the motion of the penetrator lies only in the plane including the spinning gun barrel.

Among the observed/calculated parameters, the penetration path length and impact angle may have the largest errors, mainly because we need the assumption on the impact point  $P$  for these values. The uncertainty of the impact point, however, is less than  $\pm 7.5$  cm because the crater diameter produced by the present experiments was less than 15 cm. When the penetration path length calculated by the above method is 50 cm, the corresponding error on this parameter is estimated to be  $\pm 1$  cm from the geometrical relation. Even if the target's surface roughness of 2 cm is added to the uncertainty of impact point, the maximum error of the penetration path length is only 3 cm. The error of the impact angle or inflection angle is estimated to be less than 3.5 degrees because the distance between the center of rotation wheel and the target's surface is about 1.2 m.

## 3. RESULTS

All the experimental conditions and results of 145 shots are summarized in Table 1. Although the impact velocity range of the experiments is 80 to 200 m/s which are lower than the predicted impact velocity of the LUNAR-A penetrator, the deceleration (and deceleration load) in the present experiments are approximately in the same range as that encountered in the real LUNAR-A penetrator. In the following, we focus our discussion on the effects of the nose shape of the penetrator and the attack angle on penetration characteristics. We believe that those experimental data can be used to assess the penetration dynamics of the LUNAR-A penetrator, if a proper care is taken for a scaling law.

### 3.1. NOSE SHAPE EFFECT

In this section, we select only the data of the zero attack-angle from Table 1 in order to see the effect of the nose shape on penetrator dynamics. Figures 8a and 8b show the penetration path-length of three kinds of the cone-nose penetrators with respect to the impact velocity. Although the mass of the models is known to affect the penetration path-length, we neglect its effect here because of small variation of the mass in the present experiments. Figures 8a and 8b indicate that the penetration path length increases with the impact velocity, though its effect in the case of the oblique impact (Figure 8b) is less obvious. We do not know at present why the effect of impact velocity on the path-length is so weak in the case of oblique impacts. Figures 8a and 8b also show that the penetration path-length is not significantly affected by  $\lambda$  of the cone-nose both for normal and oblique impact. Considering the cross-sectional area of nose-tip for the  $\lambda = 0.3$  being three times as large as that for  $\lambda = 0.1$ , this result is rather remarkable. The weak dependence of  $\lambda$  on the penetration path-length may indicate that the streamlines of the target soil around the penetrator are not affected by the truncation of the cone-tip of the penetrator. A relevant observation on this fact is that we always find a hard conic soil in front

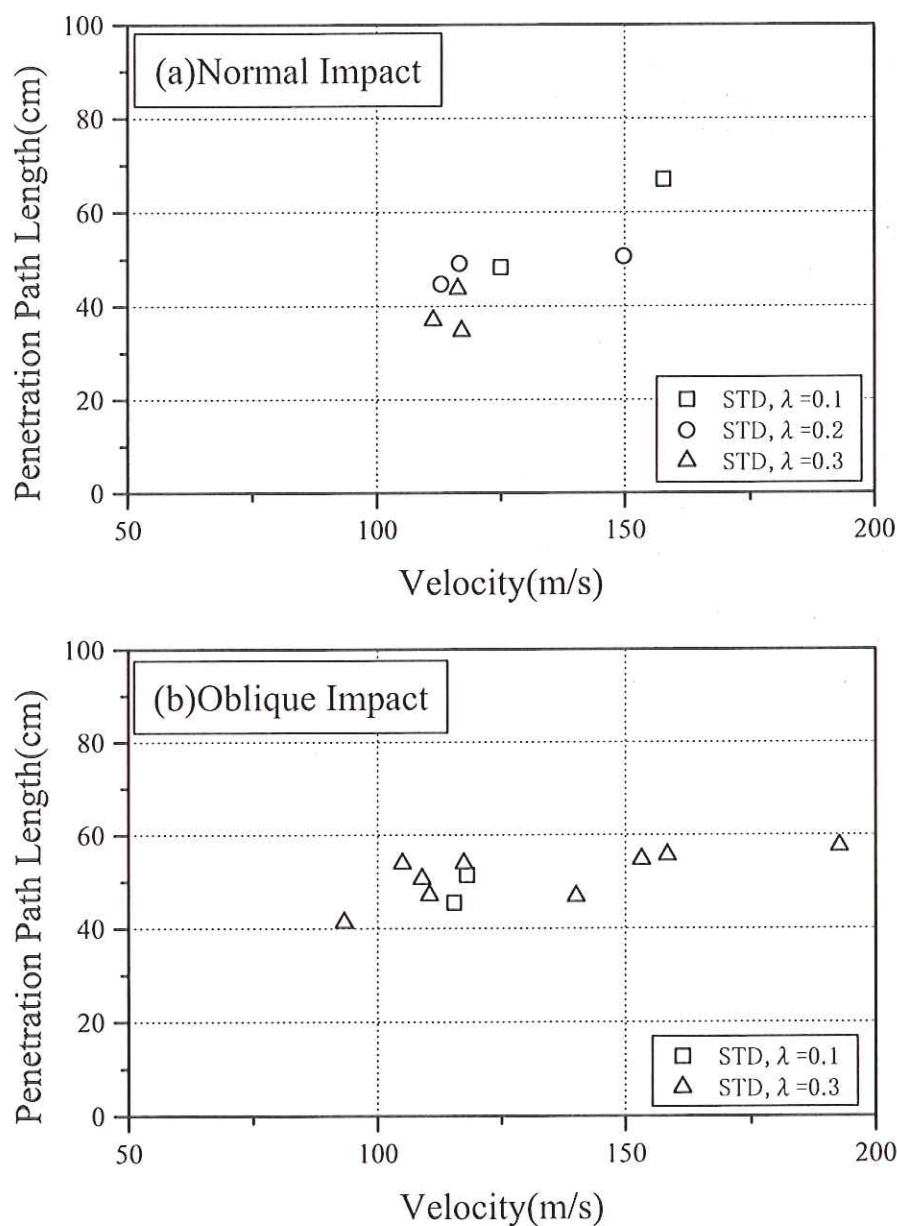


Fig. 8. Variation of the penetration path length for cone-nose penetrators with impact velocity: (a) normal impact; (b) oblique impact of  $50 \pm 3^\circ$ .

of the truncated nose of the penetrator when we recover the penetrator after the experiment.

Comparison of Figures 8a with 8b shows the effect of impact angle on the penetration path-length. Figure 8b includes the data of impact angles of  $\theta = 50 \pm 3^\circ$ . As for the cone-nose penetrators, no significant difference in path length can be seen between normal and oblique impacts; in both cases, the penetration path lengths are  $\sim 40$  cm at  $v = 100$  m/sec and  $\sim 60$  cm at  $v = 150$  m/sec.

Figures 9a and 9b show the penetration path length of three kinds of the ogive-nose penetrators with respect to the impact velocity. It indicates that the penetration path-length increases with the impact velocity. The dependence of the path-length on the impact velocity is less clear in the case of the normal impact (Figure 9a). This is probably due to the limitation of depth of the sand target. In the present experiments, we used the sand target to a depth of about 70 cm. Although the target sand



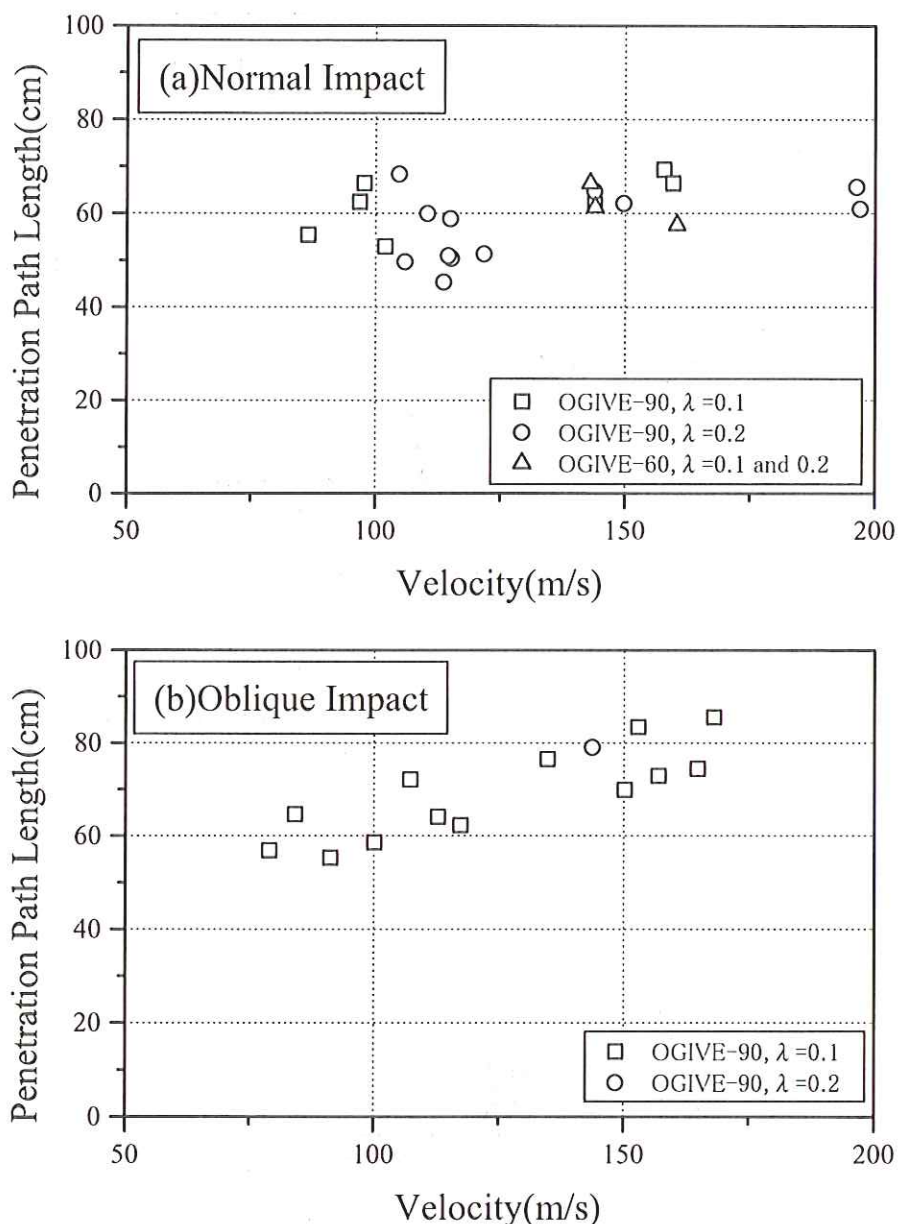


Fig. 9. Variation of the penetration path length for ogive-nose penetrators with impact velocity: (a) normal impact; (b) oblique impact of  $50 \pm 3^\circ$ .

was made as homogeneous as possible in terms of the hardness, the bottom layer might have been very hard because of the weight of overlying sand and compaction by vibration of the rotation wheel. This inference is also confirmed by the measurement of hardness distribution in the target. As shown in Figure 4, the cone penetrometer data indicates the existence of hard layer as a sudden increase of resistant force at the depth of 55 cm to 65 cm. Therefore the hard layer at the bottom of the target box may have prevented the projectile from penetrating much deeper and it will explain that the path-length in the case of the normal impact at a high-velocity range seems to be saturated at a depth of  $\sim 65$  cm.

On the other hand, the penetrator could not reach the bottom layer even at a high velocity impact ranging from 120 to 170 m/s, in the case of oblique impacts of  $\theta \sim 50^\circ$ . Therefore the data shown in

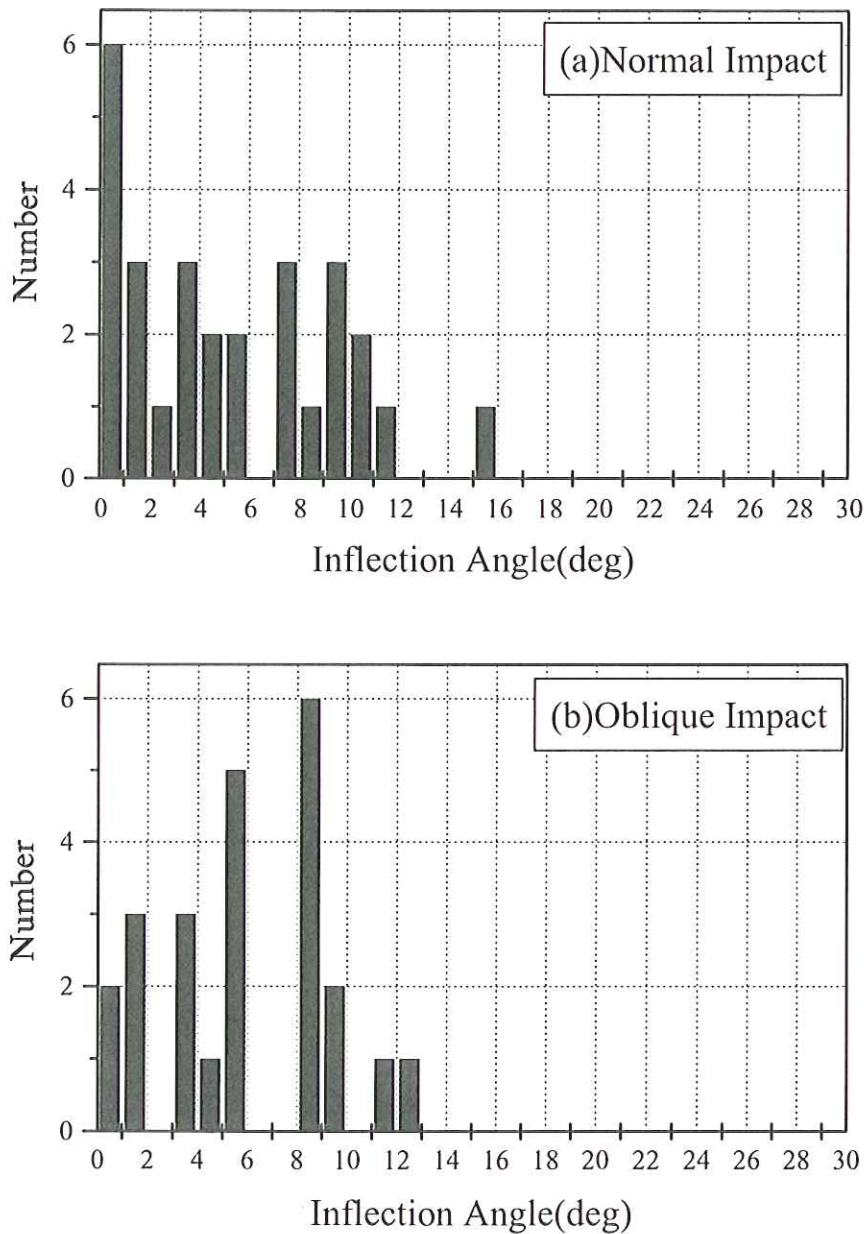


Fig. 10. Histogram distributions of inflection angle with zero attack impact: (a) normal incidence; (b) oblique impact of  $50 \pm 3^\circ$ .

Figure 9b should be used to infer the effect of impact velocity on the path-length, rather than Figure 9a.

Comparing Figure 8 with Figure 9, it is clear that the ogive-nose penetrators penetrate 1.3 to 1.5 times deeper than the cone-nose ones under the same velocity range. We think that the streamlined nose shape provides a more gradual deceleration than the conic nose and the ogive-nose penetrators penetrate deeper into the target material.

As is mentioned earlier, the course of the penetrator movement in the target sand deviates from a straight line and the attitude of the penetrator at the rest position differs from the original one. In Figures 10a and 10b, we show the histogram of the degree of inflection in terms of  $\Delta\phi$  defined in equation (5). The data in Figure 10 include the data on the cone-nose and the ogive nose. We did not



observe any significant effects of the nose shape on this inflection angle, though we observed a truncated-nose penetrator shows smaller inflection than that with non-truncated cone-nose penetrators [8]. The data for the oblique impact evidently have a peak between  $5^\circ$  and  $10^\circ$ , while the data for normal incidence are distributed around zero. This slight difference may reflect the effect of a torque applied on the nose tip just after initial contact at the oblique impact. But the absolute values of inflection angle are almost within  $10^\circ$  for both normal incidence and oblique impact. This suggests that the oblique impact does not have a significant effect on penetration trajectory.

### 3. 2. EFFECT OF ATTACK ANGLE

Figure 11 shows a cross sectional view of the penetrator which came to rest in the sand box for three cases of different attack angle,  $\alpha$ . Considering that the penetrator mass, nose shape, and impact velocity are about the same among the three experimental runs, this figure clearly shows the influence of attack angle on penetration characteristics. In cases of the normal impact with zero attack angle, the body axis of penetrator model which came to rest coincides nearly with the impact direction within  $15^\circ$ . But Figure 11 indicates that the existence of only a few degrees attack angle results in the deflection of penetration trajectory and in the large inclined stop angle from the normal. Also, it can be seen that the depth of emplacement becomes shallower with increasing in the attack angle.

As illustrated in Figure 11, the penetration path-length is also affected by the attack angle. Figures 12a to 12d show how the penetration path length changes with the attack angle. The results in cases

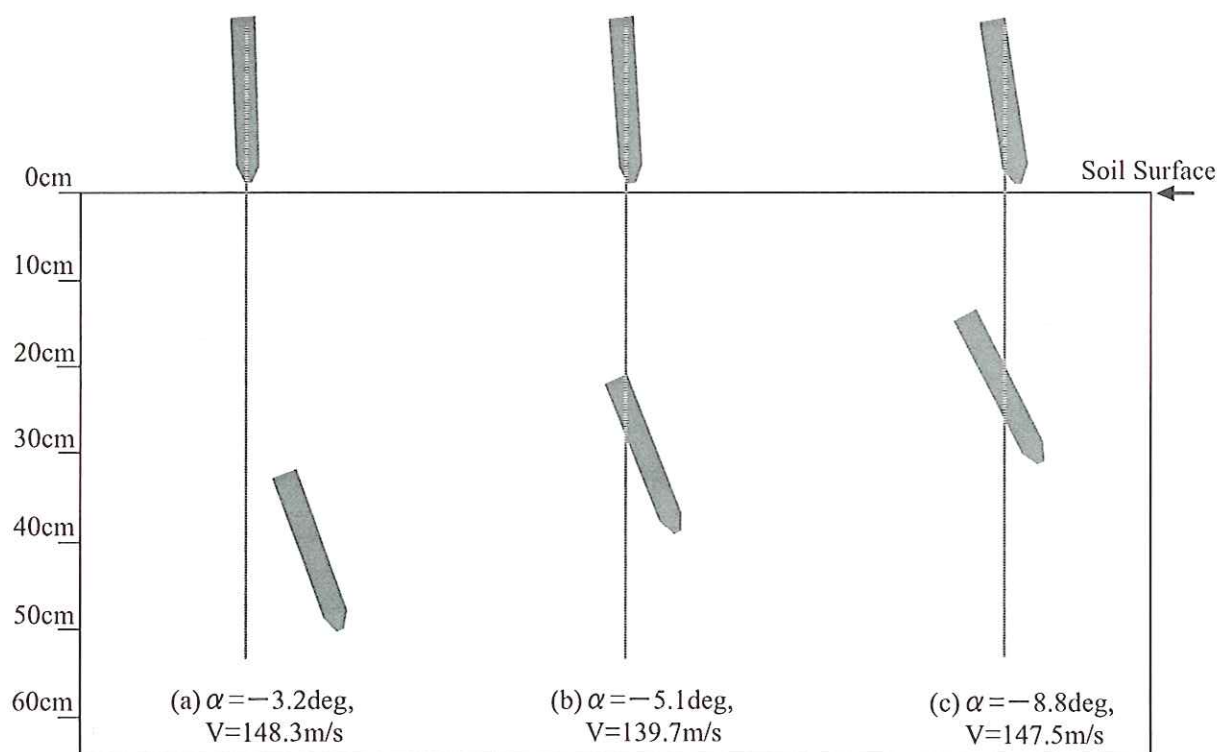


Fig. 11. Schematic cross sectional view of the location and stop angle with the case of non-zero attack impact in Runs of (a) No. 3, (b) No. 8, and (c) No. 45. The three plots are offset by 50 cm horizontally for clarification and dotted lines indicate the impact direction. The size of STD,  $\lambda = 0.3$  penetrator model is also shown to scale.

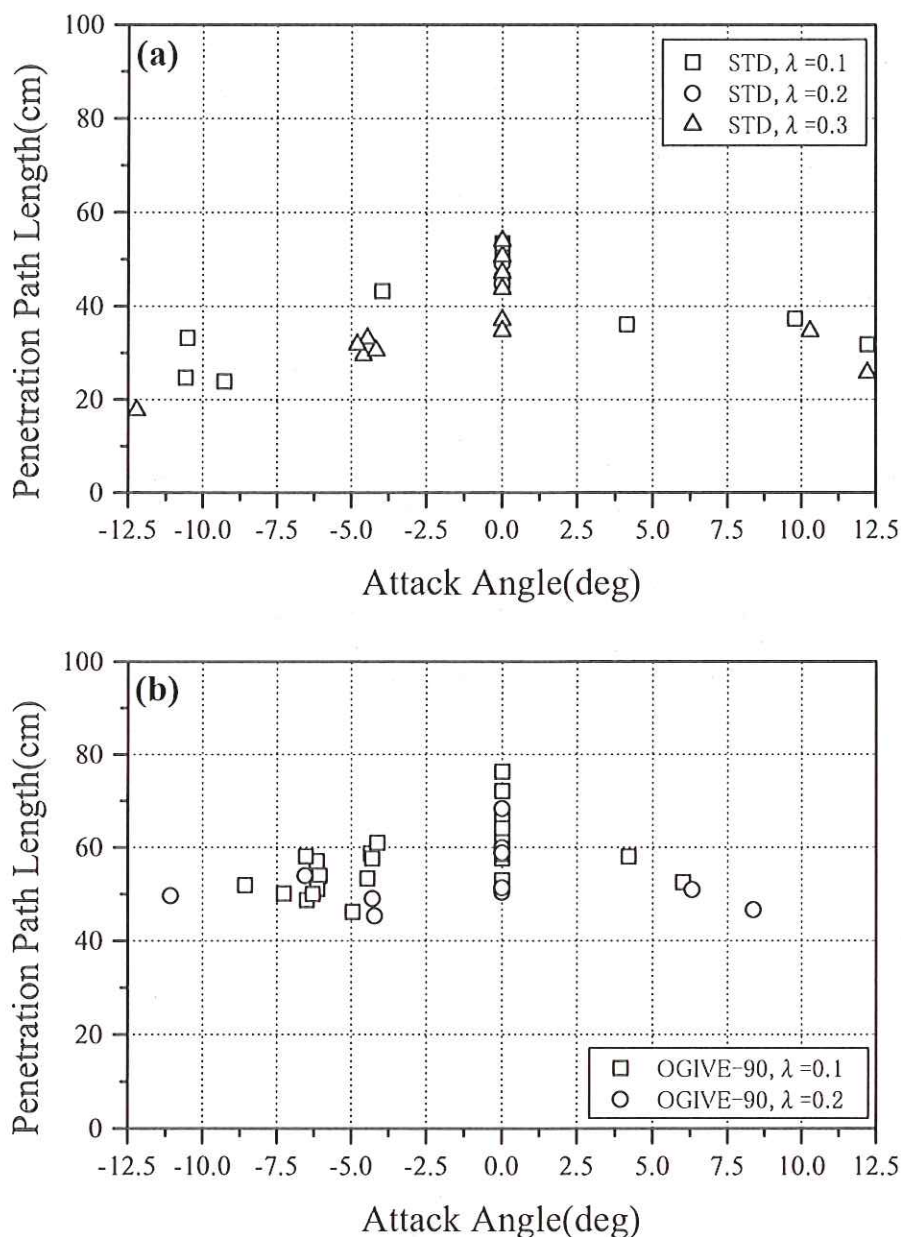
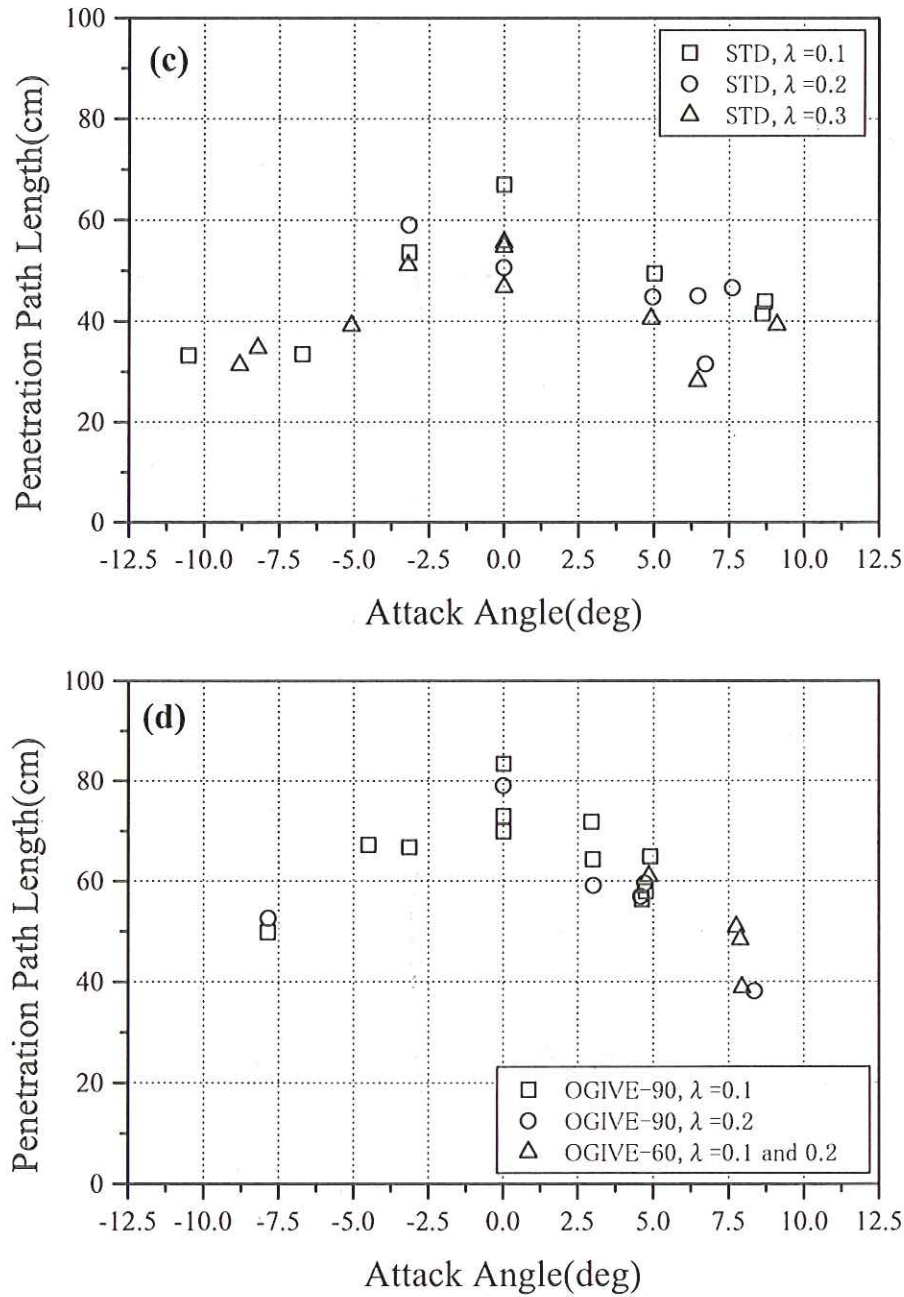


Fig. 12. Variation of the penetration path length with attack angle: (a) conical nose at  $100 \leq V \leq 120$  m/s; (b) ogive nose at  $100 \leq V \leq 120$  m/s; (c) conical nose at  $140 \leq V \leq 160$  m/s; (d) ogive nose at  $140 \leq V \leq 160$  m/s (Figs. 12 (c) and 12 (d) are shown in the next page.).

that the projectiles impacted at the velocities of 100 to 120 m/s are presented in Figures 12a and 12b, while the data at the velocities of 140 m/s to 160 m/s are presented in Figures 12c and 12d. For the projectiles of all types, the penetration path length decreases as the attack angle increases. However, even if a projectile impacts at non-zero attack angle, the ogive-nose penetrators penetrate deeper than the cone-nose penetrators under the same velocity range.

The variation of the inflection angle with attack angle is shown in Figures 13a and 13b, including the results of normal impacts with zero attack angle. As expected, an increase in attack angle enhances the deflection from the impact direction. There is a linear correlation between the attack angle and the





inflection angle for all models. The slope for each of penetrator's nose shapes by the least square fitting from experimental data is as follows;

$$\Delta\phi = 3.3\alpha + 0.5 \text{ (STD, } \lambda = 0.1), \quad (6)$$

$$\Delta\phi = 3.0\alpha + 0.3 \text{ (STD, } \lambda = 0.3), \quad (7)$$

$$\Delta\phi = 4.6\alpha + 2.2 \text{ (OGIVE-90, } \lambda = 0.1), \quad (8)$$

$$\Delta\phi = 3.5\alpha + 1.6 \text{ (OGIVE-90, } \lambda = 0.2). \quad (9)$$

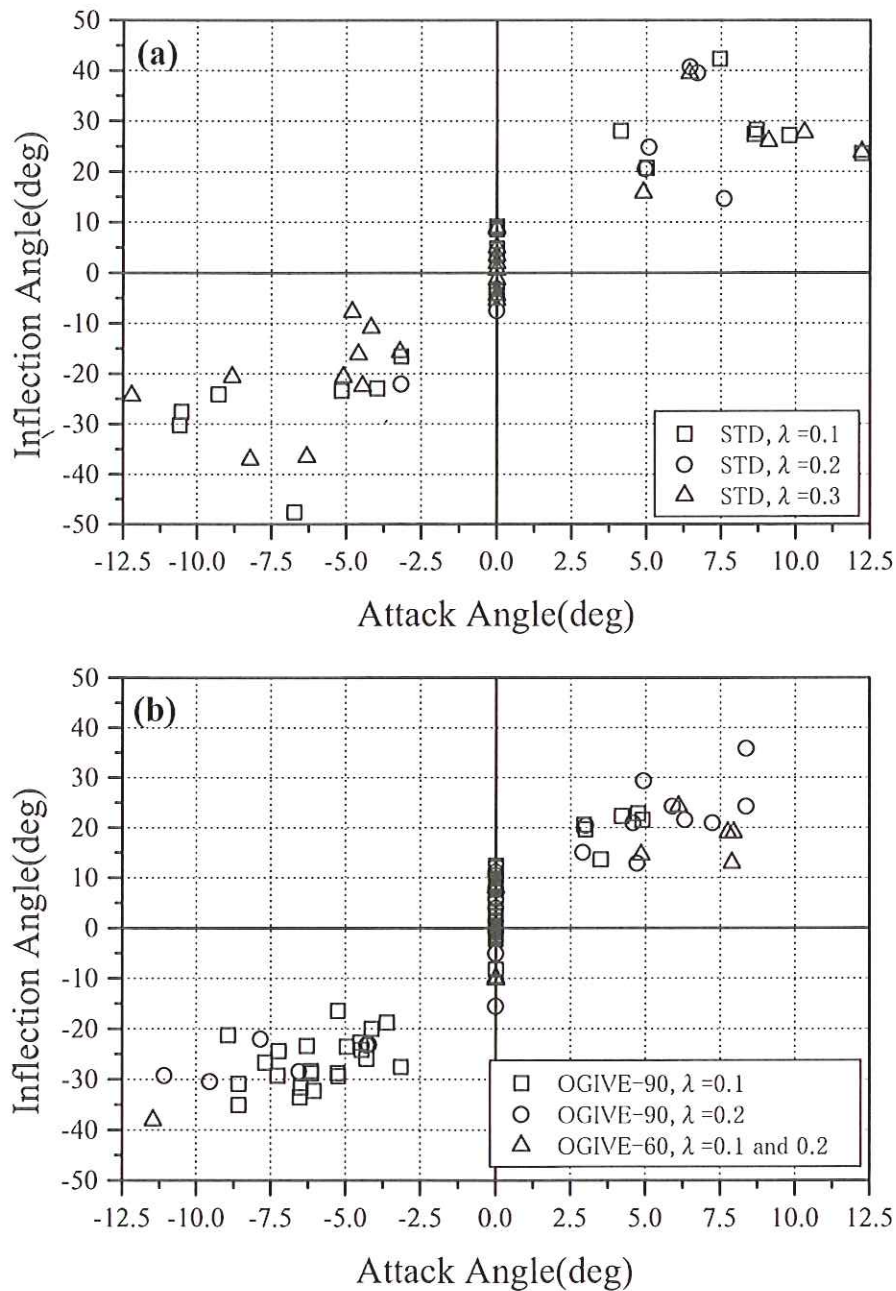


Fig. 13. Variation of the inflection angle with attack angle: (a) conical nose; (b) ogive nose.

The inflection angle for STD  $\lambda = 0.3$  is the smallest of all. This indicates that the truncation of the nose tip is efficient to stabilize the penetration orientation. But the degree of the differences observed in the relationship between the inflection angle and the impact velocity for various nose-shapes is not very significant. Considering the behavior shown in Figures 12a and 12b, i.e., deeper penetration for an ogive nose than that of the cone-shape nose, the penetrator with the ogive nose may be preferred to the penetrator with the cone-shape nose.



#### 4. CONCLUSION

We made the impact experiments of the scale-models of the LUNAR-A penetrator into lunar analogue soil and investigated the effects of the nose-shape and attack angle at impact on the penetration characteristics. The results indicate that the ogive-nose penetrator penetrates deeper than the conic nose one and that the torque applied on the penetrator in the case of non-zero attack angle changes the penetration depth and inflection angle significantly.

Although prediction of the dynamical characteristics for a real-size penetrator on the basis of the present experimental data is beyond the scope of this report, it should be emphasized here that a large attack angle might change the penetration characteristics (depth of emplacement and inflection angle) significantly. Therefore, to minimize the attack angle at the actual flight, a great care should be taken in the design of the separation mechanism from the carrier spacecraft and of the attitude control system. Moreover the uncertainty of the depth of emplacement and of the stop angle due to an inevitable occurrence of the finite attack angle must be considered in hardware and software design of the science instruments onboard LUNAR-A penetrator.

We also hope that the present experimental results provide important information to optimize a design of planetary penetrator in the future.

#### 5. ACKNOWLEDGMENTS

We would like to thank Prof. M. Kohno of Research Division for Space Propulsion, ISAS, for his support of constructing the gun facility and target sand used in the present experiment. We greatly acknowledge technical assistance from Mr. S. Yasuda, Mr. S. Sato, and Mr. S. Hirayama of Engineering Support Department of ISAS, and Mr. K. Kobayashi and Mr. Y. Uchida of Space Operations Department of ISAS. Without their generous assistance in various aspects of the experiments, the present experiment could not have been completed.

#### REFERENCES

- [1] Allen, W. A., E. B. Mayfield, and H. L. Morrison: Dynamics of a projectile penetrating sand, *J. Appl. Phys.*, 28, 370-376, 1957.
- [2] Young, C. W.: Depth prediction for earth penetrating projectiles, *J. Soil Mech. Found. Div. Am. Soc. Civ. Eng.*, 95, 803-817, 1969.
- [3] Murff, J. D., and H. M. Coyle: Prediction method for projectile penetration, *J. Soil Mech. Found. Div. Am. Soc. Civ. Eng.*, 99, 1033-1037, 1973.
- [4] Forrestal, M.J., and V. K. Luk: Penetration into soil targets, *Int. J. Impact Eng.*, 12, 427-444, 1992.
- [5] Carrier, W. D. III, G. R. Olhoeft, and W. Mendell: Physical Properties of the Lunar Surface, in *Lunar Sourcebook*, edited by G. H. Heiken, D. T. Vaniman, and B. M. French, Cambridge University Press, 475-594, 1991.
- [6] Carrier, W. D. III: Lunar soil grain size distribution, *The Moon*, 6, 250-263, 1973.
- [7] Mitchell, J. K., W. N. Houston, W. D. Carrier III, and N. C. Costes: Apollo Soil Mechanics Experiment S-200. Final report, NASA CR-134306, Space Science Laboratory Series 15, issue 7, Univ. of California, Berkeley, 1974.
- [8] ISAS Lunar Penetrator Team: Report of the 9th Penetrator Impact Test, SES-TD-92-005, The Institute of Space and Astronautical Science, 1-122, 1992 (in Japanese).